Investigation of the diameter-dependent piezoelectric response of semiconducting ZnO nanowires by Piezoresponse Force Microscopy and FEM simulations

Thomas Jalabert, Manojit Pusty, Mireille Mouis, Gustavo Ardila

Investigation of the diameter-dependent piezoelectric response of semiconducting ZnO nanowires by Piezoresponse Force Microscopy and FEM simulations

Thomas Jalabert*, Manojit Pusty, Mireille Mouis and Gustavo Ardila

Univ. Grenoble Alpes, Univ. Savoie Mont Blanc, CNRS, Grenoble INP, IMEP-LaHC, F-38000 Grenoble, France.

*E-mail: thomas.jalabert@ grenoble-inp.fr

ABSTRACT

Semiconducting piezoelectric nanowires (NWs) are promising candidates to develop highly efficient mechanical energy transducers made of biocompatible and non-critical materials. The increasing interest in mechanical energy harvesting makes the investigation of the competition between piezoelectricity, free carrier screening and depletion in semiconducting NWs essential. To date, this topic has been scarcely investigated because of the experimental challenges raised by the characterization of the direct piezoelectric effect in these nanostructures. Here we get rid of these limitations using the PFM technique in DataCube mode and measuring the effective piezoelectric coefficient through the converse piezoelectric effect. We demonstrate a sharp increase in the effective piezoelectric coefficient of vertically aligned ZnO NWs as their radius decreases. We also present a numerical model which quantitatively explains this behavior by taking into account both the dopants and the surface traps. These results have a strong impact on the characterization and optimization of mechanical energy transducers based on vertically aligned semiconducting NWs.

1. INTRODUCTION

Piezoelectricity manifests more strongly in nanowires (NWs) of some semiconductors as compared to the bulk [1] which makes nanowires particularly attractive for energy transduction applications such as strain sensing or mechanical energy harvesting [2–4]. Among other piezoelectric semiconductors such as GaN, AlN or CdS, zinc oxide (ZnO) presents several advantages due to its biocompatibility, relative abundance and variety of growth methods [5–12]. This is an asset compared to conventional piezoelectric dielectrics made of lead compounds or critical materials such as Cd, Al or Ga. Because of their large surface to volume ratio, the effects of the surface on the piezoelectric behavior of NWs can be prominent. For instance, large piezoelectric coefficients have been predicted due to the reorganization of surface atoms [13–17]. However, this only manifests at small scales (few nm diameter NWs) and is therefore very difficult to observe experimentally. At larger scales, the semiconducting character of the NWs comes into play. On the one hand, strong piezoelectric damping is expected in doped NWs because of the screening of the electric polarization by free charge carriers [18]. On the other hand, this screening can be effectively counteracted in nanostructures with a large surface to volume ratio such as nanoporous films [19–21] and NWs [22,23] by the surface Fermi-level pinning mechanism resulting from large densities of surface traps [24]. The interplay between the geometry and the semiconducting properties of

piezoelectric semiconducting NWs is then of particular interest for the optimization of piezoelectric devices integrating such NWs.

However, there is a lack of experimental results concerning the effect of diameter on the electromechanical properties of piezoelectric semiconducting NWs, especially at the nanoscale. Piezoresponse Force Microscopy (PFM) is the perfect tool to probe the converse piezoelectric effect on individual NWs [25–27], but no study of the effect of the NWs dimensions has been reported with this technique. Up to now, the most convincing results about the influence of NW diameter on the piezoelectric response of individual NWs have been obtained very recently by probing the direct piezoelectric effect of GaN NWs under constant normal force [28]. Despite the consolidating PMMA matrix, the thinnest NWs were highly strained, with buckling and twinning/twisting effects leading to complex strain and polarization fields. The analysis was carefully restricted to the more rigid nanowires that were subjected to axial strain. It showed an increase in the conversion efficiency as the NW radius decreases [28], consistently with the effect of surface Fermi-level pinning [24]. It should be noted also that in these experiments the top of the NWs has been metallized which has the advantage of improving the contact of the AFM tip to the NW but prevents local inhomogeneity to be probed. Impedance mismatch [28], clamping by the PMMA matrix [26] and dispersion of NWs lengths [29] have been also shown to play a role, aside from the effect of NWs radii, in direct piezoelectric conversion.

In terms of modelling, only a few models of piezoelectric semiconducting NWs accounted for their semiconducting character. The influence of the NWs length and diameter on the direct piezoelectric effect has been evaluated for vertically integrated nanogenerators (VINGs) [29]. The surface trap density and doping level used for the simulations were based on their expected range for a variety of growth methods. performance of vertically integrated nanogenerators (VINGs) has been evaluated. for a variety of growth methods based on their expected range of doping levels and density of surface traps [29]. As for the converse piezoelectric effect, very few models have included the PFM configuration and they neglected free charge carriers and surface traps [25] although the latter has been shown to greatly affect the piezoelectric properties [24].

In this work, we performed PFM measurements on vertically aligned ZnO NWs grown by CBD (Chemical Bath Deposition) with a given length and various radii and found a strong diameter dependence of the piezoelectric coefficient on the NW radius. Numerical simulations accounting for both the piezoelectric and semiconducting (i.e. doping and surface traps) properties of these nanowires quantitatively supported our results.

2. EXPERIMENTAL AND SIMULATION DETAILS

ZnO NWs were grown from different seed layers deposited on indium tin oxide (ITO) coated silicon substrates using CBD growth technique [30]. The seed layers had different thicknesses ranging from 10 to 150 nm and were deposited by e-beam evaporation either at room temperature (RT) or at 100°C. Figure S1 shows X-ray diffraction (XRD) patterns of the seed layers showing the presence of ZnO in the c-axis preferred orientation. After growth, the NWs were found to be vertically aligned and with a length close to 3 µm as evidenced by Figure 1 and Figures S2 and S3.

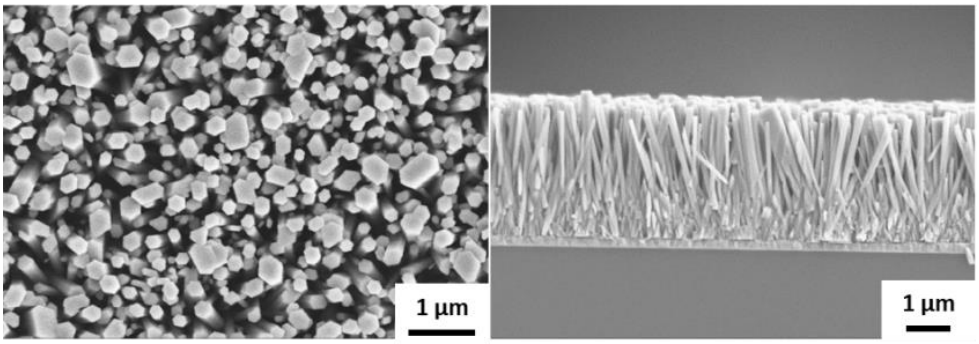

Figure 1. Top (left panel) and side (right panel) SEM views of a typical sample made of ZnO NWs grown from a 40 nm ZnO seed layer deposited at room temperature on an ITO coated Si substrate.

We performed Piezoresponse Force Microscopy (PFM) measurements with an Atomic Force Microscope (AFM ; Dimension Icon from Bruker) to probe the local piezoelectric properties on individual ZnO NWs. The absence of insulating matrix between the grown NWs prevented clamping artifacts during PFM characterization [26]. The specific DataCube mode (DCUBE-PFM, Bruker) avoids collisions and lateral bending of the vertically grown NWs with the tip by retracting the tip before it is laterally moved from one pixel of the AFM image to another [5]. The vertical force exerted by the tip on the NWs is small enough to prevent NW buckling (see Supplementary Information). We used platinum coated silicon tips (PtSi-NCH from Bruker) with a spring constant in the range 43-50 N/m and a resonance frequency between 204 and 497 kHz. We recorded with the AFM tip the sample's deformation due to the application of an AC PFM modulation voltage of 5 V between the sample's bottom electrode and the tip (grounded). The PFM amplitude and phase are the tip oscillations amplitude at the frequency of the PFM modulation and the phase shift between the tip mechanical oscillations and the PFM modulation voltage, respectively. We set the PFM modulation frequency in the range 10-15 kHz and ensured that the piezoresponse amplitude and phase were frequency independent to avoid parasitic piezoelectric amplitude magnification as previously reported [27,31,32]. The significant stiffness of the tip also prevented cantilever buckling and significantly reduced electrostatic interference with piezoresponse [33].

We also performed numerical simulations using the finite element method within the COMSOL Multiphysics environment. We used the *Electrostatics* and *Solid Mechanics* modules with user defined modifications of the set of equations to account for free charge carriers and surface traps. We performed static simulations as in previous works [27,32] because the PFM amplitude is independent of the PFM modulation frequency in our experiments. Unlike [25] we did not consider the Schottky contact between the tip and the NW because of the two following differences with [25] in our experiments. First, no current was flowing between the tip and the sample. Secondly, the piezoresponse signal did not contain other harmonics than the one at the PFM modulation frequency, while higher order harmonics would have been generated as a result of Schottky contact non-linearity [25]. The simulated 2D structure is sketched on Figure 2. It consists in a ZnO seed layer substrate, a ZnO NW and a metallic tip in air environment. The seed layer thickness t_{seed} and the NW length L_{NW} were set to 50 nm and 3 µm, respectively. The influence of these parameters was found to be much smaller than that of the radius and

is thus discussed in Supplementary Information (see Figures S4 and S5). The AFM tip was modeled by a 20 nm thick cylinder with 20 nm radius on top of the ZnO NW. In order to save computing resources we used a 2D axisymmetric simulation.

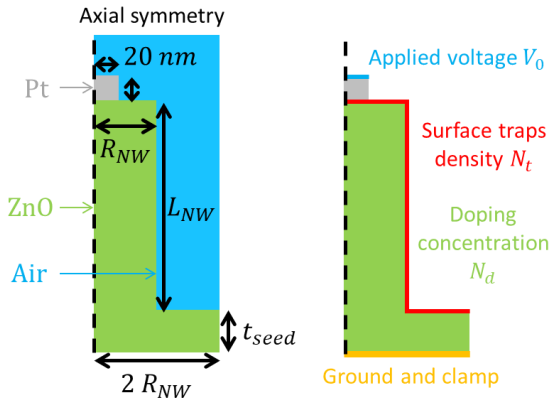

Figure 2. Schematics of the 2D axisymmetric numerical simulation of the deformation of a single ZnO NW within COMSOL environment. (a) Geometry, dimensions and materials. (b) Electrical and mechanical boundary conditions.

The bottom seed layer was mechanically clamped, and we assumed that the tip was not affecting the mechanical motion of the NW. The mechanical properties of ZnO used in our model are summarized in Table S1 in Supplementary Information. In order to reflect the metallic behaviour of the tip, we set its electric permittivity to a large value (1000) compared to the one of ZnO (see Table S1). The electric potential was set to zero on the bottom electrode in order to ensure the semiconductor neutrality in the seed layer and we applied a voltage V_0 to the tip.

The following coupled equations were used to account for the piezoelectric and semiconducting behaviour of the NWs:

$$[\boldsymbol{\sigma}] = [\mathbf{c}][\boldsymbol{\varepsilon}] - [\mathbf{e}]^{\mathbf{T}}[\mathbf{E}] \quad (1)$$

$$[\mathbf{D}] = [\mathbf{e}][\boldsymbol{\varepsilon}] + [\boldsymbol{\kappa}][\mathbf{E}] \quad (2)$$

where [σ] is the stress matrix, [ε] is the strain matrix, [E] is the electric field vector, [D] is the electric displacement vector, [c] is the elasticity matrix, [κ] is the dielectric constant matrix and [e] is the piezoelectric coefficient matrix. The two matrices $[\mathrm{e}]$ and $[\mathrm{e}]^{\mathrm{T}}$ introduce the coupling between piezoelectric and semiconductor physics, and correspond to direct and inverse piezoelectric effect, respectively.

The local free carrier densities and the average doping concentrations were included in the local density of charge (ρ) in Poisson's equation:

$$\boldsymbol{\nabla} \cdot \mathbf{D} = \rho = \mathrm{e}(\mathrm{p} - \mathrm{n} + \mathrm{N_d} - \mathrm{N_a}), \quad (3)$$

where n, p, N_a and N_d are the densities of electrons, holes, acceptor atoms, and donor atoms, respectively. Electron and hole concentrations were functions of the local electric potential and of the band structures of the ZnO material.

Finally, we introduced a uniform trap density N_t at the ZnO surface (see Figure 1b), leading to a surface charge density:

$$Q_s = -e^2 N_t (V_s - \varphi_{if}), \quad (4)$$

where V_s is the surface potential and φ_{if} the difference between Fermi level and intrinsic level [29] (see Supplementary Information 4). For the sake of simplicity, we made the hypothesis that the traps were ideally slow, with a charge that remained frozen when the applied voltage was varied. The boundary condition at ZnO interfaces was thus based on the local surface voltage obtained in the initial state, so that the surface charge was position-dependant but time-independent.

The piezoresponse amplitude was then computed as the top surface displacement resulting from a variation of the potential applied to the tip from an initial value $V_0^i = 0$ to a final value $V_0^f = -1\ V$. We defined the effective piezoelectric coefficient d_{33}^{eff} as the piezoresponse amplitude divided by $|V_0^f - V_0^i|$.

3. RESULTS AND DISCUSSION

Figure 3 shows the topography, tip-sample adhesion force, piezoresponse amplitude and phase maps recorded on a typical sample. All our NWs exhibited Zn polarity as demonstrated by the positive phase of the piezoresponse [31] (see Figure 3d).

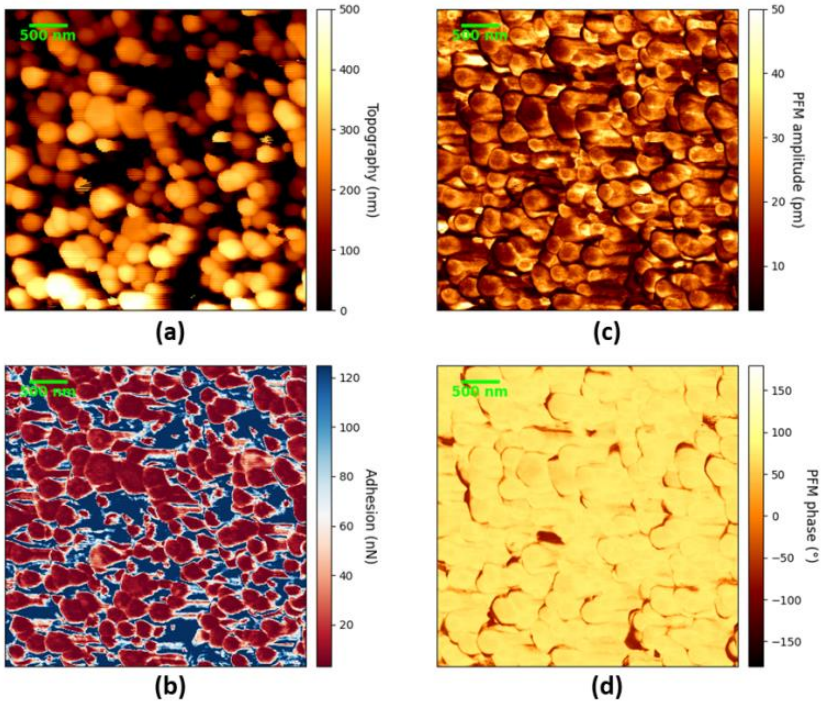

Figure 3. (a) Topography (b) adhesion force (c) PFM amplitude and (d) PFM phase distributions measured on ZnO NWs grown from a 150 nm ZnO seed layer deposited at room temperature on an ITO coated Si substrate.

We extracted the PFM data corresponding only to the top surface of ZnO NWs, and studied their dependence as a function of the NW radius. To do so, we defined the following methodology. Consistently with previous work [27], we noticed that the top

surface of the NWs corresponds to a lower adhesion force between the tip and the NW (see Figure 3). We therefore filtered the PFM data on the NWs using an adhesion force threshold. Then, we selected hexagonal areas corresponding to each NW using the topography image (see Figure 4a). Finally, we used this data to compute the radius of the NWs and their associated mean piezoelectric properties. The convolution between the tip and the NWs may result in a small systematic overestimate of the NW radius of a value approximately equal to the tip radius of curvature (< 25 nm). The effective piezoelectric coefficient d_{33}^{eff} was computed as the ratio between the recorded piezoresponse amplitude and the applied AC voltage amplitude. Figure 4b shows the resulting dependence of the effective d_{33}^{eff} coefficient as a function of NW radius R_{NW}. Vertical and horizontal error bars correspond to the standard deviation of the d_{33}^{eff} distribution corresponding to each NW and to the size of a pixel of the AFM image, respectively.

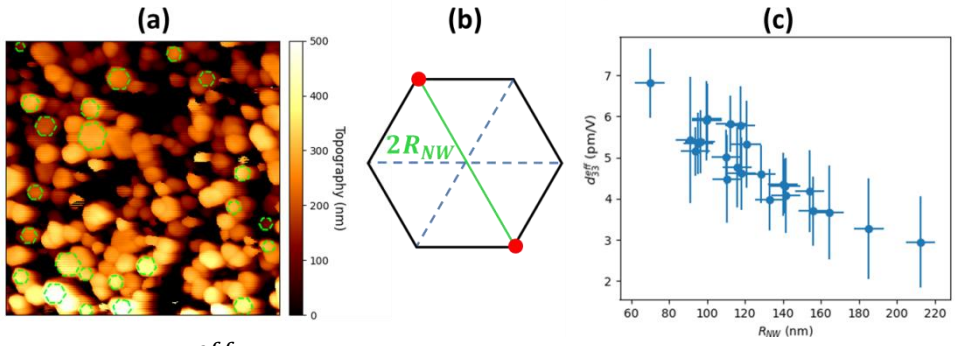

Figure 4. Effective d_{33}^{eff} coefficient measured on the NWs top surface as a function of NW radius. (a) Topography image with the position of the analyzed NWs in green. (b) Scheme of the hexagonal shape of the NWs and definition of radius. (c) Effective piezoelectric coefficient versus NW radius computed from the piezoresponse data recorded in the pixels within the hexagonal areas depicted in (a) and with an adhesion lower than 60 nN (see text). Same sample as in Figure 3.

Figure 5 displays the effective d_{33}^{eff} coefficient as a function of R_{NW} measured on samples grown on different seed layers. 120 NWs from 6 different samples were analyzed. A clear general trend was found, with an increase of d_{33}^{eff} as R_{NW} is lowered. For the largest radii, d_{33}^{eff} seems to reach a plateau. In addition, the samples with a thicker seed layer showed smaller d_{33}^{eff} coefficient. In contrast, no clear trend was observed as the seed layer deposition temperature was modified. Our results confirm the trend found in recent works [27,28] where a smaller NW radius led to a larger piezoresponse. However, since PFM characterizes the converse piezoelectric effect instead of the direct piezoelectric effect, there was no intentional force applied on the NWs in this mode. Therefore there was no need for a PMMA matrix to mechanically consolidate the NWs which were not prompt to parasitic flexion by contrast with previous work [28].

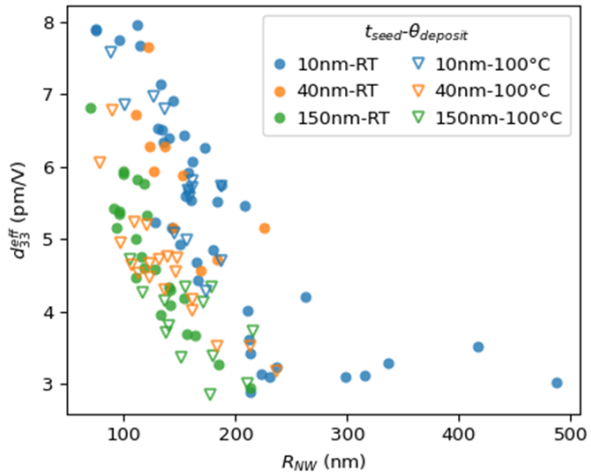

Figure 5. Effective d_{33} coefficient measured by PFM on the NWs top surface as a function of NW radius for several samples with different seed layer thicknesses t_{seed} and deposition temperatures $\theta_{deposit}$.

In order to test the relevance of the experimentally observed trend, we evaluated the radius dependence expected from simulations in the PFM configuration for different doping concentrations and trap densities. The simulation results are superimposed to experimental data in Figure 6. The numerical solution quantitatively predicted a strong variation of d_{33}^{eff} as a function of R_{NW}. A sharp increase of d_{33}^{eff} was predicted for a critical value of the radius R_{NW}^{c}. At large radii, d_{33}^{eff} reached a plateau corresponding to the value computed for a thin film (dashed lines, see Supplementary Information for more details). The calculated values of both d_{33}^{eff} and R_{NW}^{c} depended on doping concentration and surface traps density. A good agreement between experimental data and simulations was obtained for N_{it} in the range $10^{12} - 10^{13} eV^{-1}.cm^{-2}$ and N_d in the range $1 - 5 \times 10^{17}\ cm^{-3}$. We tested as well the model of an insulating NW without semiconducting properties (dotted lines). This model also predicted an increase of d_{33}^{eff} when R_{NW} was lowered. However, its origin was purely electrostatic. Because of the small tip size as compared to the NW radius, an increase of the radius leads to a larger radial distribution of the electric field and therefore a lower deformation along the NW axis [25]. Finally, this simplified model was unable to capture the sharpness of the increase observed experimentally and predicts a larger d_{33}^{eff} coefficient than the semiconducting model because it does not include free charge carrier screening effects.

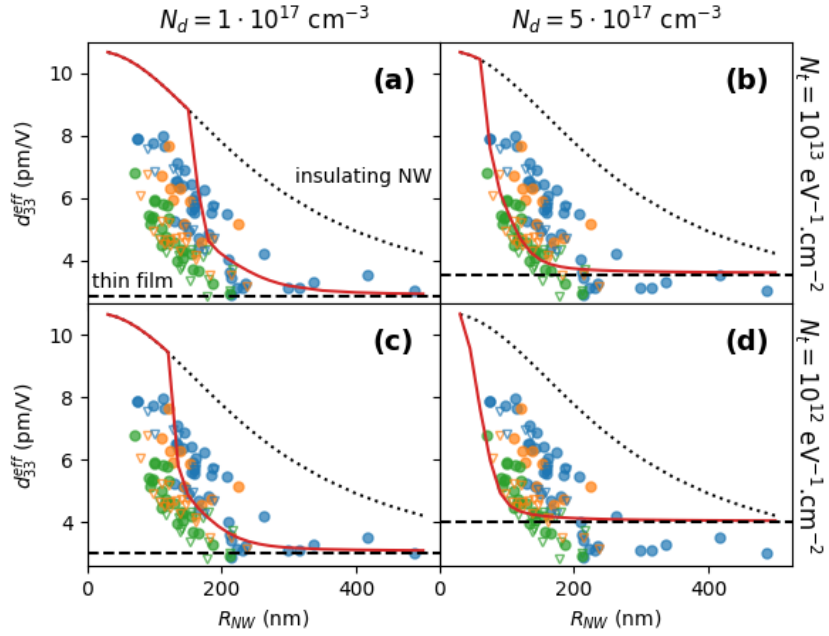

Figure 6. d_{33}^{eff} coefficient versus NW radius. Dots: same experimental data as in Figure 4. Solid line: numerical results for a doping concentration $N_d = 1 \times 10^{17} cm^{-3}$ (a), (c) and $N_d = 5 \times 10^{17} cm^{-3}$ (b), (d) and a surface trap density $N_t = 10^{12} eV^{-1}.cm^{-2}$ (a), (b) and $N_t = 10^{13} eV^{-1}.cm^{-2}$ (c), (d). Dashed lines are the numerical results for a thin film of same thickness and with the same semiconducting properties than the associated panel. Dotted lines are the numerical results for a NW without semiconducting properties (insulating).

The sharp increase of d_{33}^{eff} at small radius was explained by the depletion of the core of the NW from its free carriers as evidenced by Figure 7. For wide NWs, whose core was neutral, free carriers were able to screen the piezoelectric potential all along the NW. In contrast, narrow NWs were fully depleted, resulting in a large increase of the NW vertical displacement (see electric field induced displacement and electric potential distribution in Figure S6 and Figure S7) and therefore of d_{33}^{eff}. The threshold between these two situations arose when the depletion depth reached R_{NW}. This occurred for NW radii between 150 and 200 nm depending on the doping level and the surface trap density. For $N_d = 10^{17} cm^{-3}$ and $N_t = 10^{13} eV^{-1}.cm^{-2}$, full depletion was analytically computed to be around 150 nm [29] consistently with our numerical computations.

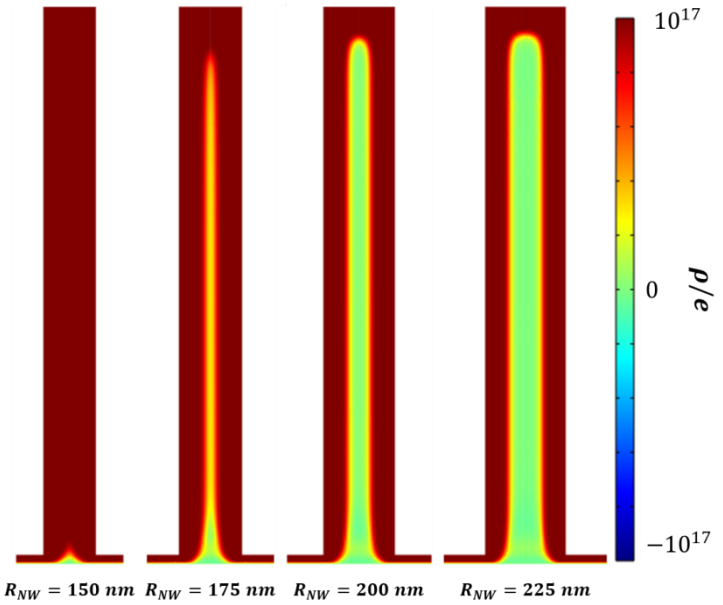

Figure 7. Charge density ρ (in units of e) for $R_{NW} = 150$, 175, 200 and 200 nm with a doping concentration $N_d = 10^{17} cm^{-3}$ and a surface trap density $N_t = 10^{13} eV^{-1}.cm^{-2}$.

The doping level strongly depends on the growth technique. According to previous reports [34], it is expected to range from 5×10^{17} to $5 \times 10^{18}\ cm^{-3}$ and 5×10^{18} to $1 \times 10^{19}\ cm^{-3}$ for CBD with O polarity and CBD with Zn polarity, respectively. The surface trap density of ZnO NWs grown by CBD method has not been extensively investigated. However, because of a rougher surface, it is expected to be larger than the one obtained by CVD (whose trap density is about $10^{12} eV^{-1}.cm^{-2}$) [29]. Our NWs were grown by CBD and exhibited Zn polarity (see Figure 2d). The value of the trap density used in our simulations is therefore consistent with the one expected from literature. As for the doping density, it is about one order of magnitude smaller than the one reported for Zn polarity. A small overestimate of the NW radius due to tip convolution effects would slightly increase the doping level required to fit our simulations with experimental data. However, the few reports about doping concentration in ZnO NWs rely on the analysis of resistivity measurements with several approximations which limit the model used for parameter extraction [34]. In this paper, both carrier concentration and mobility were taken as spatially constant whereas they can be affected by surface states. Carrier density was deduced from four-point resistivity measurements on individually contacted NWs which had been dispersed on a Si/SiO_2 substrate beforehand. However, with such a configuration, flatband conditions are not guaranteed and the extracted carrier density may be significantly larger than doping level due to positive charges at SiO_2 interface. These approximations may explain the difference between the doping concentration that have been evaluated in the literature for these growth conditions and the one from our simulations. This also stresses the interest of developing an experimental technique to directly probe the carrier concentration in these nanostructures.

We also simulated the effect of the NWs length on the d_{33}^{eff} coefficient. The variations in the NWs lengths are typically smaller than 500 nm (see topography image in Figure 3a) and the NWs are about $L_{NW} = 3.2$ µm long (see Figure S3). We therefore computed the d_{33}^{eff} coefficient as a function of R_{NW} for $L_{NW} = 3$ µm and $L_{NW} = 3.5$ µm (see Figure S4) showing that such variations in L_{NW} induce a small change in d_{33}^{eff} (typically less than 10%). This suggests that the dispersion of the d_{33}^{eff} coefficient measured on the same sample for the same radius (see Figure 4c) may be attributed to different NW lengths. Finally, our simulations showed that the seed layer thickness only slightly affects the simulated d_{33}^{eff} coefficient (see Figure S5) through a small voltage drop along the NW due to a smaller distance between the tip and the bottom electrode. We therefore think that the effect of the seed layer on the d_{33}^{eff} coefficient is not due to different depletion profiles in the seed layer. In contrast, changing the seed layer affects the growth process and may result in different semiconducting properties for the NWs which would in turn directly affect their piezoelectric performances as shown by the strong dependence of d_{33}^{eff} on both N_d and N_{it} (see Figure 6). The measuring of these semiconducting properties will be part of further investigations.

CONCLUSIONS

We measured the vertical deformation of vertically aligned ZnO NWs by PFM. By using the DataCube mode which prevents collisions between the tip and the NWs during the scan we extracted the effective piezoelectric coefficient through the converse piezoelectric effect. In contrast with the conventional characterization of nanocomposites based on ZnO NWs through the direct piezoelectric effect, our technique does not require the application of a large force on the NWs to measure a significant piezoresponse nor the use of an insulating matrix to consolidate the NWs. This prevents parasitic effects such as clamping or buckling. We clearly evidenced at the nanoscale a strong increase of the effective piezoelectric coefficient as the NWs radius decreases and a limited impact of the NWs length in the explored range of values. These observations remained valid for a large number of NWs grown by CBD on seed layers with different thicknesses. We quantitatively supported our observations by a numerical model which included for the first time the presence of both dopants and surface traps in the PFM configuration.

Thanks to its large spatial resolution and its versatility with respect to the variety of semiconducting materials and growth methods, our experimental method provides a powerful tool to provide optimization guidelines piezoelectric devices based on semiconducting NWs. Our numerical model also allows a better understanding of the physical mechanisms at stake by considering both piezoelectricity and semiconducting phenomena. Additional refinements considering the unique mechanical properties of NWs could also be included. Finally, this work shows that further experimental investigations about carrier concentration and trap density would be essential to quantify more accurately the role of these parameters in transducers based on piezoelectric semiconducting NWs.

AUTHOR CONTRIBUTIONS

TJ performed the experiments, analysed the data and performed the numerical simulations. MP performed the CBD growth of the samples. GA supervised the project and found the funding supporting this work. TJ, MP, MM and GA wrote the manuscript. All authors have read and agreed to the published version of the manuscript.

ACKNOWLEDGMENTS

This work has been partly supported by the ANR projects SCENIC (under grant agreement ANR-20-CE09-0005) and LATINO (under grant agreement ANR-21-CE50-0026) from the French Ministry of Research. It also have been partly supported by the European Union's Horizon 2020 research and innovation programme projects PULSECOM (under grant agreement No 863227) and ENABLES (under grant agreement no 730957).

CONFLICTS OF INTEREST

The authors declare no conflict of interest.

DATA AVAILABILITY STATEMENT

All data that support the findings of this study are included within the article (and any supplementary files).

REFERENCES

1. Minary-Jolandan, M.; Bernal, R.A.; Kuljanishvili, I.; Parpoil, V.; Espinosa, H.D. Individual GaN Nanowires Exhibit Strong Piezoelectricity in 3D. *Nano Lett.* **2012**, *12*, 970–976, doi:10.1021/nl204043y.
2. Hu, Y.; Lin, L.; Zhang, Y.; Wang, Z.L. Replacing a Battery by a Nanogenerator with 20 V Output. *Advanced Materials* **2012**, *24*, 110–114, doi:10.1002/adma.201103727.
3. Wang, Z.; Pan, X.; He, Y.; Hu, Y.; Gu, H.; Wang, Y. Piezoelectric Nanowires in Energy Harvesting Applications. *Advances in Materials Science and Engineering* **2015**, *2015*, e165631, doi:10.1155/2015/165631.
4. Panth, M.; Cook, B.; Zhang, Y.; Ewing, D.; Tramble, A.; Wilson, A.; Wu, J. High-Performance Strain Sensors Based on Vertically Aligned Piezoelectric Zinc Oxide Nanowire Array/Graphene Nanohybrids. *ACS Appl. Nano Mater.* **2020**, *3*, 6711–6718, doi:10.1021/acsanm.0c01150.
5. Schmidt-Mende, L.; MacManus-Driscoll, J.L. ZnO – Nanostructures, Defects, and Devices. *Materials Today* **2007**, *10*, 40–48, doi:10.1016/S1369-7021(07)70078-0.
6. Nobis, T.; Kaidashev, E.M.; Rahm, A.; Lorenz, M.; Lenzner, J.; Grundmann, M. Spatially Inhomogeneous Impurity Distribution in ZnO Micropillars. *Nano Lett.* **2004**, *4*, 797–800, doi:10.1021/nl049889y.
7. Yao, B.D.; Chan, Y.F.; Wang, N. Formation of ZnO Nanostructures by a Simple Way of Thermal Evaporation. *Appl. Phys. Lett.* **2002**, *81*, 757–759, doi:10.1063/1.1495878.
8. Wu, J.-J.; Liu, S.-C. Low-Temperature Growth of Well-Aligned ZnO Nanorods by Chemical Vapor Deposition. *Advanced Materials* **2002**, *14*, 215–218, doi:10.1002/1521-4095(20020205)14:3<215::AID-ADMA215>3.0.CO;2-J.
9. Park, W.I.; Kim, D.H.; Jung, S.-W.; Yi, G.-C. Metalorganic Vapor-Phase Epitaxial Growth of Vertically Well-Aligned ZnO Nanorods. *Appl. Phys. Lett.* **2002**, *80*, 4232–4234, doi:10.1063/1.1482800.

10. Peulon, S.; Lincot, D. Cathodic Electrodeposition from Aqueous Solution of Dense or Open-Structured Zinc Oxide Films. *Advanced Materials* **1996**, *8*, 166–170, doi:10.1002/adma.19960080216.
11. Vayssieres, L.; Keis, K.; Lindquist, S.-E.; Hagfeldt, A. Purpose-Built Anisotropic Metal Oxide Material: 3D Highly Oriented Microrod Array of ZnO. *J. Phys. Chem. B* **2001**, *105*, 3350–3352, doi:10.1021/jp010026s.
12. Consonni, V.; Lord, A.M. Polarity in ZnO Nanowires: A Critical Issue for Piezotronic and Piezoelectric Devices. *Nano Energy* **2021**, *83*, 105789, doi:10.1016/j.nanoen.2021.105789.
13. Yan, Z.; Jiang, L. Modified Continuum Mechanics Modeling on Size-Dependent Properties of Piezoelectric Nanomaterials: A Review. *Nanomaterials* **2017**, *7*, 27, doi:10.3390/nano7020027.
14. Yvonnet, J.; Mitrushchenkov, A.; Chambaud, G.; He, Q.-C.; Gu, S.-T. Characterization of Surface and Nonlinear Elasticity in Wurtzite ZnO Nanowires. *Journal of Applied Physics* **2012**, *111*, 124305, doi:10.1063/1.4729545.
15. Hoang, M.-T.; Yvonnet, J.; Mitrushchenkov, A.; Chambaud, G. First-Principles Based Multiscale Model of Piezoelectric Nanowires with Surface Effects. *Journal of Applied Physics* **2013**, *113*, 014309, doi:10.1063/1.4773333.
16. Agrawal, R.; Espinosa, H.D. Giant Piezoelectric Size Effects in Zinc Oxide and Gallium Nitride Nanowires. A First Principles Investigation. *Nano Lett.* **2011**, *11*, 786–790, doi:10.1021/nl104004d.
17. Espinosa, H.D.; Bernal, R.A.; Minary-Jolandan, M. A Review of Mechanical and Electromechanical Properties of Piezoelectric Nanowires. *Advanced Materials* **2012**, *24*, 4656–4675, doi:10.1002/adma.201104810.
18. Romano, G.; Mantini, G.; Carlo, A.D.; D'Amico, A.; Falconi, C.; Wang, Z.L. Piezoelectric Potential in Vertically Aligned Nanowires for High Output Nanogenerators. *Nanotechnology* **2011**, *22*, 465401, doi:10.1088/0957-4484/22/46/465401.
19. Waseem, A.; Jeong, D.K.; Johar, M.A.; Kang, J.-H.; Ha, J.-S.; Lee, J.K.; Ryu, S.-W. Enhanced Piezoelectric Output of NiO/Nanoporous GaN by Suppression of Internal Carrier Screening. *Semicond. Sci. Technol.* **2018**, *33*, 065007, doi:10.1088/1361-6641/aabf5f.
20. Calahorra, Y.; Spiridon, B.; Wineman, A.; Busolo, T.; Griffin, P.; Szewczyk, P.K.; Zhu, T.; Jing, Q.; Oliver, R.; Kar-Narayan, S. Enhanced Piezoelectricity and Electromechanical Efficiency in Semiconducting GaN Due to Nanoscale Porosity. *Applied Materials Today* **2020**, *21*, 100858, doi:10.1016/j.apmt.2020.100858.
21. Kang, J.-H.; Jeong, D.K.; Ha, J.-S.; Lee, J.K.; Ryu, S.-W. Enhanced Performance of a GaN Piezoelectric Nanogenerator with an Embedded Nanoporous Layer via the Suppressed Carrier Screening Effect. *Semicond. Sci. Technol.* **2017**, *32*, 025001, doi:10.1088/1361-6641/32/2/025001.
22. Synhaivskyi, O.; Albertini, D.; Gaffuri, P.; Chauveau, J.-M.; Consonni, V.; Gautier, B.; Bremond, G. Evidence of Piezoelectric Potential and Screening Effect in Single Highly Doped ZnO:Ga and ZnO:Al Nanowires by Advanced Scanning Probe Microscopy. *J. Phys. Chem. C* **2021**, *125*, 15373–15383, doi:10.1021/acs.jpcc.1c00926.
23. Calahorra, Y.; Husmann, A.; Bourdelain, A.; Kim, W.; Vukajlovic-Plestina, J.; Boughey, C.; Jing, Q.; Morral, A.F. i; Kar-Narayan, S. Highly Sensitive Piezotronic Pressure Sensors Based on Undoped GaAs Nanowire Ensembles. *J. Phys. D: Appl. Phys.* **2019**, *52*, 294002, doi:10.1088/1361-6463/ab1386.
24. Tao, R.; Mouis, M.; Ardila, G. Unveiling the Influence of Surface Fermi Level Pinning on the Piezoelectric Response of Semiconducting Nanowires. *Advanced Electronic Materials* **2018**, *4*, 1700299, doi:10.1002/aelm.201700299.
25. Lozano, H.; Catalán, G.; Esteve, J.; Domingo, N.; Murillo, G. Non-Linear Nanoscale Piezoresponse of Single ZnO Nanowires Affected by Piezotronic Effect. *Nanotechnology* **2020**, *32*, 025202, doi:10.1088/1361-6528/abb972.

26. Jaloustre, L.; Le Denmat, S.; Auzelle, T.; Azadmand, M.; Geelhaar, L.; Dahlem, F.; Songmuang, R. Toward Quantitative Measurements of Piezoelectricity in III-N Semiconductor Nanowires. *ACS Appl. Nano Mater.* **2021**, *4*, 43–52, doi:10.1021/acsanm.0c02078.
27. Garcia, A.J.L.; Jalabert, T.; Pusty, M.; Defoor, V.; Mescot, X.; Montanino, M.; Sico, G.; Loffredo, F.; Villani, F.; Nenna, G.; et al. Size and Semiconducting Effects on the Piezoelectric Performances of ZnO Nanowires Grown onto Gravure-Printed Seed Layers on Flexible Substrates. *Nanoenergy Advances* **2022**, *2*, 197–209, doi:10.3390/nanoenergyadv2020008.
28. Gogneau, N.; Chrétien, P.; Sodhi, T.; Couraud, L.; Leroy, L.; Travers, L.; Harmand, J.-C.; H. Julien, F.; Tchernycheva, M.; Houzé, F. Electromechanical Conversion Efficiency of GaN NWs: Critical Influence of the NW Stiffness, the Schottky Nano-Contact and the Surface Charge Effects. *Nanoscale* **2022**, *14*, 4965–4976, doi:10.1039/D1NR07863A.
29. Lopez Garcia, A.J.; Mouis, M.; Consonni, V.; Ardila, G. Dimensional Roadmap for Maximizing the Piezoelectrical Response of ZnO Nanowire-Based Transducers: Impact of Growth Method. *Nanomaterials* **2021**, *11*, 941, doi:10.3390/nano11040941.
30. Garcia, A.J.L.; Sico, G.; Montanino, M.; Defoor, V.; Pusty, M.; Mescot, X.; Loffredo, F.; Villani, F.; Nenna, G.; Ardila, G. Low-Temperature Growth of ZnO Nanowires from Gravure-Printed ZnO Nanoparticle Seed Layers for Flexible Piezoelectric Devices. *Nanomaterials* **2021**, *11*, 1430, doi:10.3390/nano11061430.
31. Bui, Q.C.; Ardila, G.; Sarigiannidou, E.; Roussel, H.; Jiménez, C.; Chaix-Pluchery, O.; Guerfi, Y.; Bassani, F.; Donatini, F.; Mescot, X.; et al. Morphology Transition of ZnO from Thin Film to Nanowires on Silicon and Its Correlated Enhanced Zinc Polarity Uniformity and Piezoelectric Responses. *ACS Appl. Mater. Interfaces* **2020**, *12*, 29583–29593, doi:10.1021/acsami.0c04112.
32. Jaloustre, L.; Le Denmat, S.; Auzelle, T.; Azadmand, M.; Geelhaar, L.; Dahlem, F.; Songmuang, R. Toward Quantitative Measurements of Piezoelectricity in III-N Semiconductor Nanowires. *ACS Appl. Nano Mater.* **2021**, *4*, 43–52, doi:10.1021/acsanm.0c02078.
33. Kim, S.; Seol, D.; Lu, X.; Alexe, M.; Kim, Y. Electrostatic-Free Piezoresponse Force Microscopy. *Sci Rep* **2017**, *7*, 41657, doi:10.1038/srep41657.
34. Cossuet, T.; Donatini, F.; Lord, A.M.; Appert, E.; Pernot, J.; Consonni, V. Polarity-Dependent High Electrical Conductivity of ZnO Nanorods and Its Relation to Hydrogen. *J. Phys. Chem. C* **2018**, *122*, 22767–22775, doi:10.1021/acs.jpcc.8b07388.